Additive Manufacturing 63 (2023) 103404

Contents lists available at ScienceDirect

Additive Manufacturing

journal homepage: www.elsevier.com/locate/addma

Multi-wavelength pyrometry as an in situ diagnostic tool in metal additive manufacturing: Detecting sintering and liquid phase transitions in electron beam powder bed fusion☆

César A. Terrazas-Nájera [a,b], Alejandro Romero [a,b], Ralph Felice [c], Ryan Wicker [a,b,*]

[a] W. M. Keck Center for 3D Innovation, College of Engineering E-108, The University of Texas at El Paso, University Ave. 500 W, El Paso, TX 79968, USA
[b] Department of Aerospace and Mechanical Engineering, The University of Texas at El Paso, El Paso, TX 79968, USA
[c] FAR Associates, Macedonia, OH 44056, USA

ARTICLE INFO

Keywords:
continuous temperature and spectral emissivity measurements
in situ monitoring
radiation thermometry
powder metal processing

ABSTRACT

Radiation thermometry techniques have been implemented to measure thermal signatures in powder bed fusion (PBF) additive manufacturing (AM), including the use of imaging devices with a large field of view, to measure large areas of the powder bed with spatial discrimination, and those considered single spot devices that measure signatures from a small region. Traditionally, these techniques can be categorized as single-color (brightness) or two-color (ratio) pyrometry; imaging devices are single-color while spot devices can be either. Both techniques can be used to infer a target temperature using a priori knowledge of the emissivity or employing the graybody assumption of constant emissivity across the spectrum. However, the dynamics of PBF AM, where a concentrated heat source is employed to selectively melt powder material, lead to complex material phase transitions under non-equilibrium solidification conditions. This makes it challenging to measure accurate thermal signatures because the emissivity of the target is also constantly varying as the PBF process unfolds. In this work, we employed an established technique of multi-wavelength pyrometry in an electron beam powder bed fusion (PBF-EB) system to continuously measure temperatures and the thermal emissive behavior during sintering and melting of an Inconel 625 powder that was subjected to preheating by direct scanning with the electron beam. The measurements displayed distinctive changes in signal strength or emissivity (in the wavelength range between 1080 nm and 1640 nm) that indicated the material phase change from loose to sintered powder to molten material and finally to solidified material; these changes in signal strength/emissivity were correlated with electron microscopy observations. This work highlights the suitability of multi-wavelength (MW) pyrometry as an in situ diagnostic tool to identify thermal process signatures (i.e., absolute temperatures), and the radiative emissive behavior of the materials being processed. Several demonstrations of the use of this MW pyrometry technique as a diagnostic tool are provided, illustrating its ability to sense signal strength/emissivity differences as the material experiences changes due to its temperature, phase, morphology, and chemistry. Although spatial and temporal improvements in the technique can be pursued, the sensitivity of the approach is demonstrated, as an example, in the ability to capture the passing thermal wavefronts arising from the scanning electron beam. It is anticipated that this technique and the information it provides can be leveraged in the development of advanced techniques for thermal monitoring and process control in PBF.

1. Introduction

Powder bed fusion (PBF) additive manufacturing (AM) has evolved into production of advanced and complex metallic components with applications in highly regulated industries. For PBF AM, a laser or electron beam serves as the concentrated energy source that is used to

Abbreviations: PBF, Powder Bed Fusion; AM, Additive Manufacturing; PBF-EB, Electron Beam Powder Bed Fusion; PBF-LB, Laser Beam Powder Bed Fusion.

☆ Clear for public release: distribution unlimited.

* Corresponding author at: W. M. Keck Center for 3D Innovation, College of Engineering E-108, The University of Texas at El Paso, University Ave. 500 W, El Paso, TX 79968, USA.

E-mail addresses: caterrazas2@utep.edu (C.A. Terrazas-Nájera), rwicker@utep.edu (R. Wicker).

https://doi.org/10.1016/j.addma.2023.103404
Received 13 July 2022; Received in revised form 11 December 2022; Accepted 5 January 2023
Available online 9 January 2023
2214-8604/© 2023 The Authors. Published by Elsevier B.V. This is an open access article under the CC BY-NC-ND license (http://creativecommons.org/licenses/by-nc-nd/4.0/).

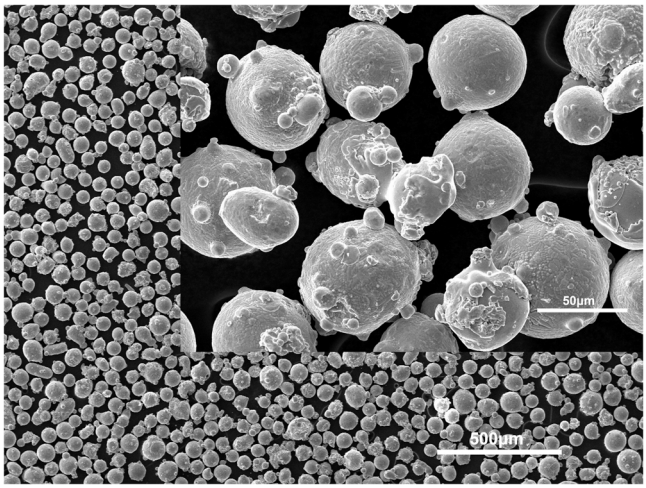

Fig. 1. SEM images of Inconel 625 powder at low (50X) magnification. Inset (500X) shows detail of individual particles.

fuse metallic powder feedstocks, layer-by-layer, into the finalized parts. During the fusion process, multiple transient phenomena are at play due to the interaction of the energy source with the powder particles resulting in non-equilibrium solidification. Monitoring and understanding of thermal process signatures during PBF can be used to establish a direct link between thermo-mechanical history that develops during processing, and the metallurgical characteristics and mechanical performance of the components produced, capturing the essence of the process-structure-property-performance (PSPP) paradigm [1–3].

Still, thermal monitoring in PBF has traditionally relied on the use of non-contact methods requiring a priori knowledge of the emissivity for brightness or single-color pyrometers that at best can be used to report a radiance temperature as a proxy for true temperature, or the application of the graybody assumption for ratio or two-color pyrometers, requiring constant emissivity across the spectrum being measured. This is the case for multiple current efforts reported in literature using both imaging and single spot radiation thermometers [4–10] applied to both laser powder bed fusion (PBF-LB) and electron beam powder bed fusion (PBF-EB). These approaches to radiation thermometry monitoring provide no information on the dynamic emissivity behavior of the targets drastically limiting the accuracy of measured thermal signatures. In truth, emissivity is a dynamic material property that varies, among other factors, according to intrinsic surface characteristics of the target under study (surface morphology, chemistry and phase of the material, material state temperature, and radiation emission wavelength). The measured temperature values can also be influenced by the measurement setup conditions (including instrument waveband or spectrum), and the absorption and emission effects from the local environment [11]. There is therefore a need to account for this dynamic variability of emissivity for a given material being formed in the powder bed, to ensure accuracy of thermal signatures measured and how these relate to the processing conditions in PBF AM.

Previously, we have reported on the use of a multi-wavelength (MW) pyrometer to directly measure the emissivity behavior during heating and melting of a region in a copper powder bed. The results obtained indicated the non-graybody behavior of the material as seen by its temporal and spectral variation of emissivity [12]. In the current work, we report on observations made employing the same MW pyrometry technique in a PBF-EB system to measure the emissive behavior for Inconel 625 during sintering and melting induced by preheating via rapid scanning using the electron beam. The emissivity measurements are correlated with scanning electron microscopy (SEM) observations that revealed changes in the surface of the heated powder bed indicative of sintering and melting for the material. While the technique presented can be employed to evaluate the emissivity variations as a function of various dependencies that include temperature, morphology, change of phase, and chemistry, the work presented here focuses on demonstrating diagnostic capabilities of MW pyrometry detecting variations in temperature, phase, and surface morphology (sintering, melting, and solidification) since any variations due to chemistry changes during processing were not isolated or measured. Whereas the MW pyrometer measures and reports signal strength rather than emissivity, the term signal strength/emissivity has been used throughout the discussion in this work. For the measurement to represent the emissivity of the target, the authors have determined that three conditions are necessary, and these conditions will be described in more detail in the description of the MW pyrometer technique and in the discussion of the results.

2. Materials and methods

2.1. Inconel 625

The powder employed in this work was Inconel 625 (Praxair Surface Technologies, USA) that was gas atomized using argon. Fig. 1 shows SEM images of the powder illustrating mostly spheroidal particles with smaller satellites. Detail for a powder particle with remnants of dendrite solidification is seen in the micrograph in the inset. The powder has an average particle size distribution ranging from 45 to 106 µm with values of d10 (47 µm), d50 (70 µm) and d90 (106 µm) as provided by the powder manufacturer. The powder's chemical composition is listed in Table 1 as per vendor specifications.

2.2. Electron beam powder bed fusion

For the current work, a GE-Arcam A2X (GE Additive, US) PBF-EB system was employed. The A2X operates under controlled vacuum (2.0×10^{-3} mbar) assisted by a constant helium bleed and under elevated temperature allowing control of the thermal conditions throughout processing. The electron beam is generated by thermionic emission using a 3 kW electron gun, and it is accelerated through a voltage potential of 60 kV. Magnetic coils are used to dynamically control the astigmatism and focus of the electron beam which has a nominal focused beam of ~250 µm. Rapid scanning with a defocused electron beam is used for an initial preheat of the deposition substrate (~950 °C for Inconel 625) and to preheat each spread layer prior to the melt scanning step using a focused beam.

2.3. Multi-wavelength pyrometry

Measurements of temperature and signal strength/emissivity were done using a FMPI SpectroPyrometer (FAR Associates, OH, USA) attached into the A2X system using a setup as described in detail in [12]. The FMPI uses an Indium-Gallium-Arsenide (InGaAs) detector to capture spectral intensity over the nominal range of 900–1700 nm with a wavelength resolution of 1.56 nm and is radiometrically calibrated in the active range from 1080 to 1637 nm.

The calibration was done using a conical IR-563 blackbody source (Infrared Systems Development Corporation, FL, USA) that itself was

Table 1
Chemical composition of Inconel 625 powder as per vendor specification.

Element	Al	B	C	Co	Cr	Cu	Fe	Mn	Mo	N	Nb + Ta	O	P	Se	Sn	Ti	Ni
wt% content	0.06	< 0.001	0.02	0.1	21.38	0.02	4	0.03	9.09	0.009	3.72	0.0126	0.002	< 0.005	< 0.001	0.06	Bal.

calibrated and traceable to the National Institute of Standards and Technology (NIST), following the procedure as detailed by Fernandez *et. al.* [12]. In short, the FMPI was calibrated by correcting the detector's spectrum to match the spectrum of the blackbody emission at 1000 °C and then verifying agreement between source and pyrometer at several other equilibrated temperatures. The calibration process was carried out with the blackbody source operating in ambient conditions; it was performed with all the elements in the process optical path, including a quartz glass that reduced transmission by ~6%. The FMPI, as configured, captures thermal radiation as spectral intensity values from a small area or spot with a diameter of 2.7 mm at the chosen focal length of 762 mm. The device employs an algorithm that self-adjusts the exposure time (within the range from 4 μs to 8 s) based on the brightness or radiation intensity of the target being measured. The intensity is summed temporally over the exposure time for each temperature calculation, and the exposure time is provided for each temperature measurement made. Spatially, measurements from the FMPI, as for ratio pyrometry in general, are primarily influenced by the highest temperature (intensity) areas within the measured spot, with variable contributions from the lower temperature (intensity) areas, as demonstrated by Ruffino [13]. The wavelength-intensity spectrum captured is used to compute a matrix of temperature values versus wavelength employing the ratio form of Planck's equation. Analysis of this matrix yields the temperature and spectral signal/emissivity. The target temperature, its standard deviation (referred to as its tolerance), and the value of signal strength (emissivity when conditions are met as discussed next), reported at 1500 nm, are calculated and stored for each measurement. The wavelength at 1500 nm was chosen for display by the manufacturer as it represents a wavelength near the center or middle of the available detector spectrum that is not affected by water vapor absorption/emission. These values are also stored in a LOG file time stamped for the exact time of collection. Raw and corrected spectral intensity and spectral signal strength/emissivity are calculated over the available wavelength range for each logged measurement and stored in separate data (DAT) files.

In this embodiment of multi-wavelength pyrometry, the signal strength is equivalent to the emissivity when the measurements are performed with the following conditions: 1) the target being measured is isothermal throughout the field of view (~2.7 mm diameter spot for this FMPI configuration), 2) the optical path is calibrated without influence from unaccounted sources of absorption or emission, and 3) there is no influence from the reflective environment. For the experiment presented in this work, condition 2) was ensured through the experimental setup and calibration, and condition 3) was met as demonstrated in our prior work [12]. Condition 1) was also met when the target was more thermally homogeneous, such as during cooldown, whereas during rapid heating the target had regions of different temperatures (intensities) over the field of view as discussed in [13] and detailed below. During scanning of the electron beam, the local heating resulted in variability in the signal strength observed typically as local oscillations in the measured values over time. Accordingly, the results will be described as signal strength/emissivity throughout the discussion, while the measurements can be considered emissivity when the three necessary conditions described above are met (i.e., most reasonably when the electron beam is not scanning the measurement region). It should further be noted that even when the beam is scanning the measurement region, the emissivity can be deduced as approximated by a value when the beam leaves the measurement region, and the temperature of the region approaches equilibrium or a more uniform temperature. Additional details of the signal strength/emissivity measurements and the requirements described above are included in the discussion of results.

2.4. Sintering and melting

Sintering is a time-dependent and thermally driven physical phenomenon evident as the coalescence of particles in a crystalline material causing the reduction of surface area and overall system energy [14]. Of the several stages undergone during sintering, the formation of necking between adjacent particles is considered the hallmark characteristic of the process. Various sintering processes are employed in manufacturing of hard to melt materials including refractory alloys and ceramics, where sintering is usually accelerated by increasing the temperature of processing. It is well established that sintering for a given material starts at temperatures greater than ~ 0.5 the melting point of the material [14, 15].

Table 2
Parameters employed in regular processing of Inconel 625 in PBF-EB.

Parameter	Preheat Stage I	Stage II	Melt
Beam speed (mm/s)	10,000	14,600	1205
Beam current (mA)	30	38	15
Focus offset (mA)	150	150	25
Repetitions	8	12	

In the regular PBF-EB process, thin layers of powder (~100 μm) are spread, followed by preheating and melt scanning. During preheating, compaction of the powder particles is achieved for each layer spread through direct preheating with a defocused electron beam. This compaction enhances conductivity and counteracts the repulsive electrostatic forces developed during electron beam scanning, allowing for processing without the detrimental powder spreading effect, which is essentially an explosion of the charged particles on the powder bed, commonly referred to as smoke [16]. Defocusing of the electron beam is achieved by controlling its spot size and astigmatism to reduce the energy delivered per unit area. For Inconel 625 as reported in this work, the parameters employed for regular processing involve a two-stage preheating step followed by a single melting step with parameters as listed in Table 2. These parameters were selected based on prior experience and available literature [2,17–20].

2.5. Experimental setup

In this work, sintering and melting were induced in the exposed surface of a powder bed that remained after a regular fabrication process using a PBF-EB system. The experimental setup follows from the work reported in [12] where the multi-wavelength pyrometer sensor was attached, at an angle of 15 degrees from the vertical, into the chamber of a commercially available PBF-EB system via a vacuum rated KF40 tube extension, allowing near-continuous observation of process thermal emissions. The schematic in Fig. 2 shows the top view of the powder bed to indicate the location of the target observed by the pyrometer sensor relative to other parts built. Also, the mid-plane section side-view helps to denote the surface of compacted powder that was preheated to observe sintering and melting using the MW pyrometer.

As can be seen in Fig. 2, a 10 mm diameter cylinder with a height of 8 mm was built while leaving its last exposed surface subsequently covered by 5 mm of powder that was compacted by preheating following fabrication of adjacent 13 mm tall cylinders. Once fabrication completed for the 13 mm tall cylinders, the machine was controlled manually to preheat the last exposed surface of the powder bed, and specifically including the compacted powder as indicated in Fig. 2. The experiment was done using a sequence of ten consecutive preheating steps of increasing power delivery achieved by increasing the beam current in the Stage I of the preheat step. The preheating steps started at 32 mA, just 2 mA above the nominal beam current used for preheating of Inconel 625 during the regular process (30 mA), and progressively increased in steps of 2 mA until 50 mA. A raster preheating strategy with a line order of 20 was employed; this means that 20 lines are skipped in between lines scanned by the electron beam. To maintain a constant energy delivery during each preheating step, the number of repetitions for Stage I were extended to a value of 100, but each preheating step was timed at ~120 s. The beam current and number of repetitions for the

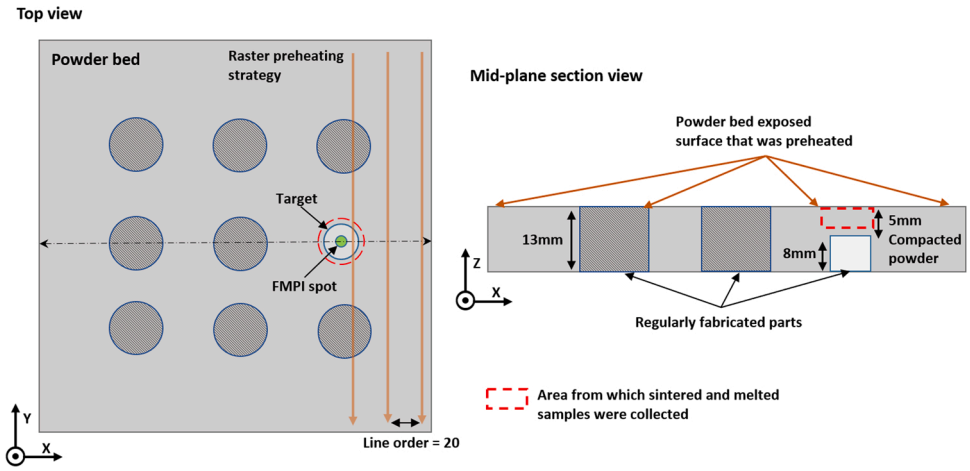

Fig. 2. Schematic showing the experimental setup employed and the raster hatching strategy used for preheating. Mid-plane section side-view indicates preheated surface that was used to observe sintering and melting using MW pyrometer.

Stage II in the preheat step were kept nominal. Following the rationale of our prior work [12], in which a copper powder bed was preheated from room temperature to the melting point, in this work the powder bed remaining after regular fabrication, exhibiting only compacted powder particles, was preheated to induce sintering and melting without powder charging and subsequent "smoke".

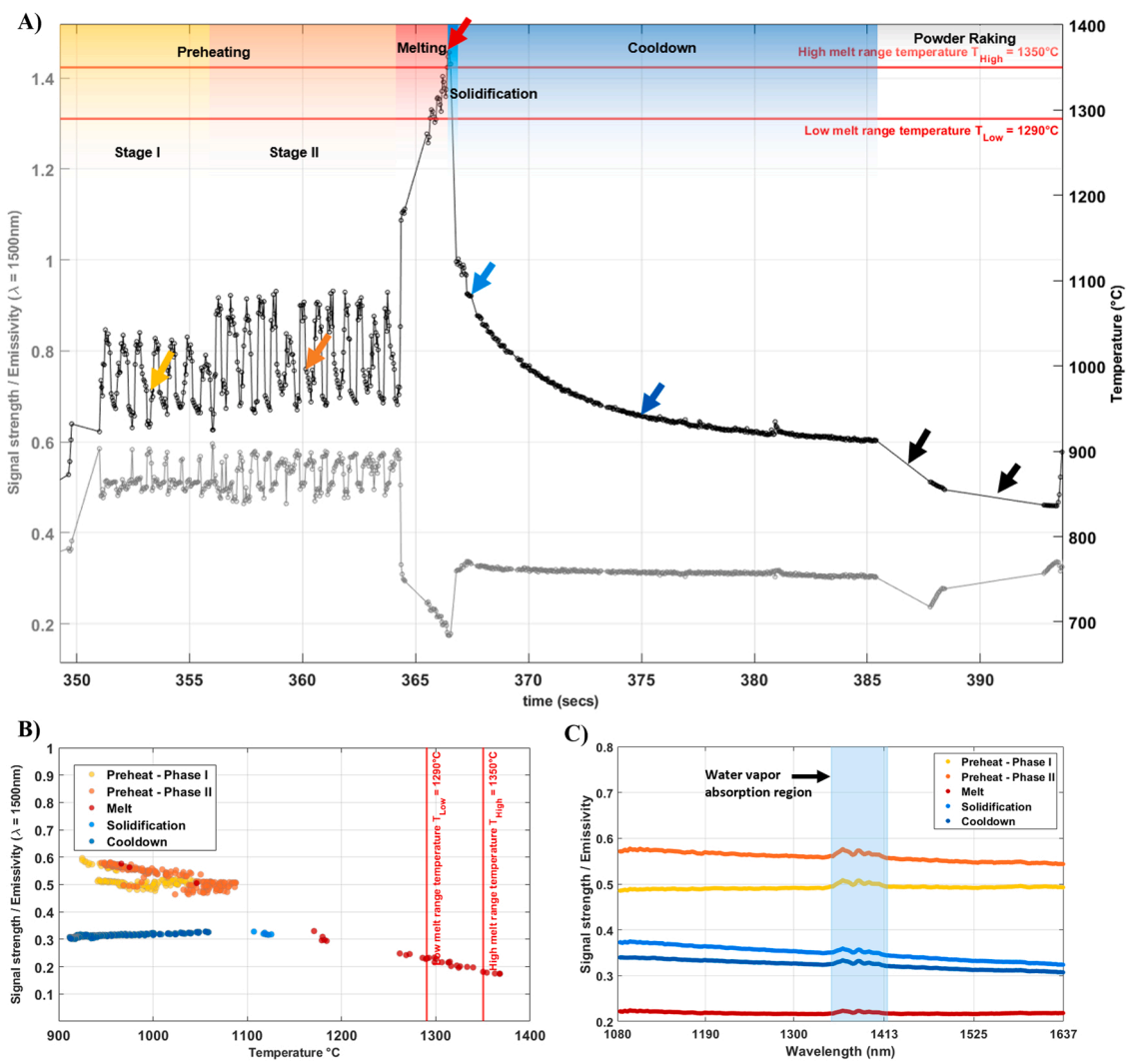

Fig. 3. A) Temperature (black) and signal strength/emissivity (gray) plot for a single melt event during PBF-EB processing of Inconel 625. Signal strength/emissivity reported is at $\lambda = 1500$ nm. B) shows the signal strength/emissivity vs temperature plot with process phases color coded. C) shows spectral emissivity in the active range of the FMPI, for selected data points indicated by colored arrows in A).

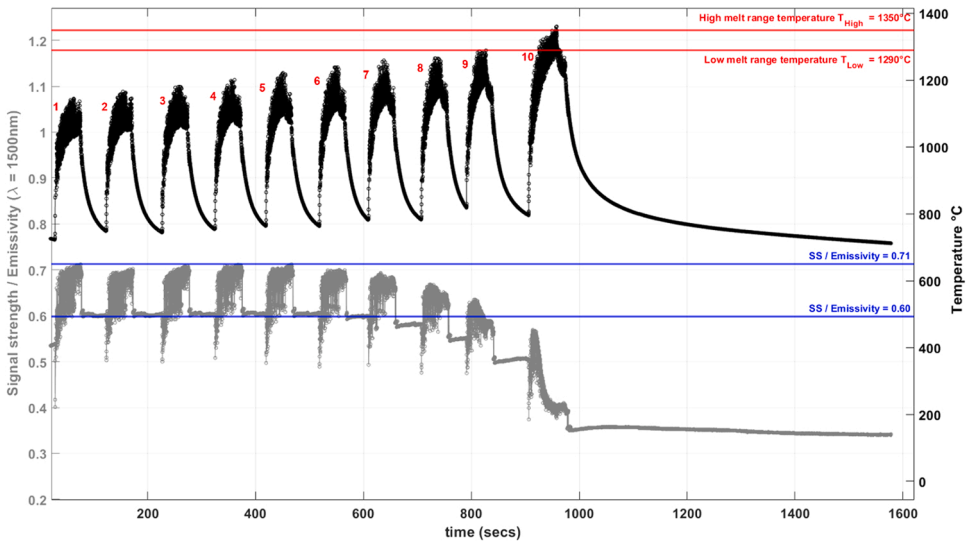

Fig. 4. Plot of temperature (black) and signal strength/emissivity (gray) for the powder bed preheating experiment.

Samples of the preheated powders were collected, prepared, and mounted for observation in a JEOL IT500LV (Tokyo, Japan) scanning electron microscope (SEM), and they were used to detail the development of sintering and melting caused by the preheating with the electron beam. Two similar experiments were performed to allow for collection of samples of sintered and melted and subsequently solidified material. The sintered sample was obtained from the first experiment corresponding to a powder bed heated using a beam current of 44 mA (seventh preheating cycle) whereas the solidified sample was collected, in the second experiment, from a powder bed that was heated up using a beam current of 50 mA (tenth preheating cycle). A third powder sample was collected that consisted of compacted powder originating from the preheating during a regular PBF-EB build carried out previously.

2.6. Temperature and signal strength/emissivity

As described above and more completely detailed in [21–23], the temperature calculation carried out by the FMPI employs Planck's ratio equation (Eq. 1), for various wavelength-intensity pairs using the radiation intensity measured from the observed target over its active spectrum. In the equation C′ corresponds to the second radiation constant, R is the ratio of intensities I_1 and I_2, and λ_1 and λ_2 are a pair of wavelengths at which intensities were measured,

$$T = \frac{C'\left(\frac{1}{\lambda_2} - \frac{1}{\lambda_1}\right)}{\ln R - 5\ln(\lambda_2/\lambda_1)} \tag{1}$$

Using this equation, the FMPI generates a matrix of temperatures from which the target temperature can be obtained by analysis, averaging and consensus. Following the calculation of temperature, tolerance, and signal strength (equivalent to emissivity in the setup described in this work when the conditions described above are met) are also computed, as recently detailed in [12]. These values are displayed and stored in a log file with the time of collection. The signal strength/emissivity stored in the log file is that at 1500 nm, a central wavelength not affected by water absorption. In addition to the log file, the instrument stores the raw spectrum, the corrected spectrum, and the spectral signal strength/emissivity for each recorded measurement in a data file. The corrected spectrum is the raw spectrum with the dark count removed and the intensity at each wavelength corrected for instrument response, as is usual in spectrometry. The correction function is obtained by measuring a known source, in this case a blackbody equilibrated at a chosen temperature, and then performing a matrix division of intensity (wavelength by wavelength) of the Planckian spectrum for the chosen temperature by the measured data. The spectral signal strength/emissivity at each wavelength is calculated by generating the expected intensity for the measured temperature and dividing it into the corrected spectrum. In this work, the data recorded in the log file produced by the FMPI was used to create scatter plots of temperature and signal strength/emissivity. The spectral signal strength/emissivity data plotted were taken directly from the data files stored by the pyrometer for each measurement. MATLAB 2021b (The MathWorks, Natick, MA) was employed for all analysis and visualization of data.

3. Results and discussion

3.1. Temperature and signal strength/emissivity

Plots of temperature and signal strength/emissivity at the wavelength of $\lambda = 1500$ nm versus time are shown in Fig. 3A) and 4 for the experiments reported in this work. Horizontal red lines in these figures indicate the reported melting range for Inconel 625 (low melt range temperature $T_{Low} = 1290$ °C, and high melt range temperature $T_{High} = 1350$ °C). Fig. 3A) shows the temperature profile for a single melting event as it occurred during the regular processing of Inconel 625 using PBF-EB. The temperatures in Fig. 3A) show the two distinctive preheating sequences (indicated by yellow and orange graded regions), elevating the temperatures to ~1045 °C, and ~1085 °C, respectively. Signal strength/emissivity values in the first preheating region are clustered at ~0.50 with local oscillations peaking at ~0.59. For the second preheating sequence, the signal strength/emissivity values exhibit more pronounced oscillations in the range from ~0.46 to ~0.59. These oscillations reveal the variability of signal strength/emissivity which, for this target, shows a dependence on temperature. The oscillating behavior exhibited correlates with the development of preheating wavefronts caused by the electron beam raster scanning strategy as used in Arcam's EBM process, an effect which is also evident in the plot for signal strength/emissivity versus temperature in Fig. 3B), showing a spread of values for signal strength/emissivity during preheating that span from ~0.45–0.60. After preheating, rapid scanning during melting (graded red region) shows an abrupt increase in temperature, from ~1050 °C to over ~1290 °C, into the melting range while the signal strength/emissivity drops sharply from ~0.60 to ~0.17. After melting, the signal strength/emissivity increases to ~0.30 during solidification (graded region in light blue). Finally, during the cooldown (graded blue region), the temperature drops from above the melting range and asymptotically approaches ~900 °C prior to the next powder raking

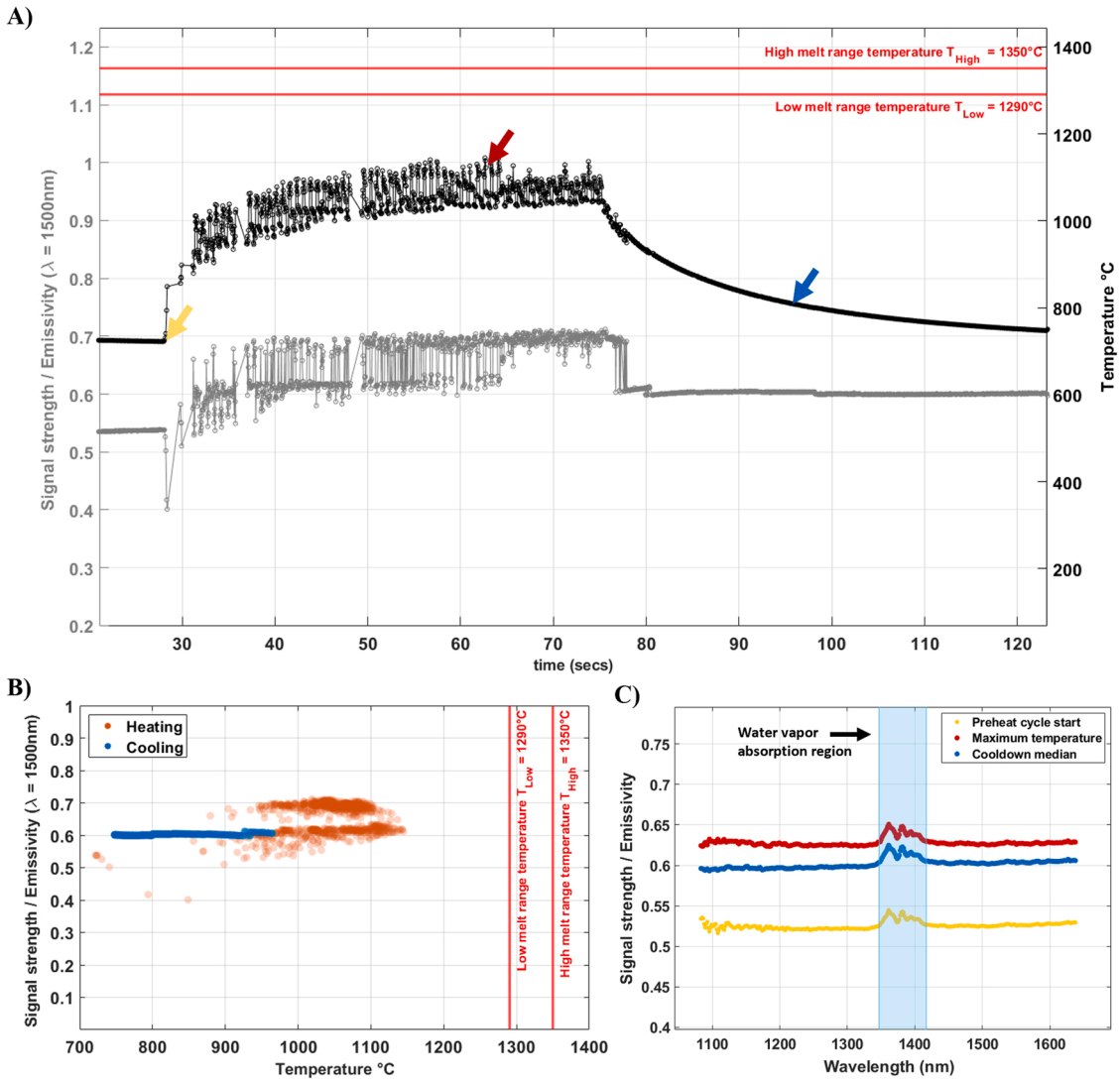

Fig. 5. A) Detail of temperature and emissivity plots for first (1st) preheating cycle. B) shows signal strength/emissivity versus temperature plot for heating and cooling, and C) shows spectral signal strength/emissivity at selected locations indicated by arrows in A).

sequence, at t ~ 385 s. During this cooldown, the signal strength/emissivity remains rather stable at ~0.31, although it is spectrally variant as shown in the Fig. 3C). The drops in temperature with corresponding fluctuations in signal strength/emissivity that occur at t ~ 385 s and t ~ 390 s, are consistent with a new layer of powder being spread. These raking events are indicated by black arrows in Fig. 3A). Also, the values for temperature and signal strength/emissivity shown in Fig. 3A) exhibit a wide range of exposure times, as dictated by varying intensity of the target. Representative values for exposure times during the melt event shown in Fig. 3A) fluctuate from 0.012 s during preheat to 0.006 s at the liquid state. The signal strength/emissivity values reported up to now in this work correspond to those at the wavelength $\lambda = 1500$ nm. As mentioned previously, the FMPI can capture the spectral variation of emissivity in the active range of 1080–1637 nm, as was demonstrated in [12]. Fig. 3C) shows plots for spectral variation of the signal strength/emissivity at five selected observations (indicated by color coded arrows) selected from Fig. 3A). The data points selected for this plot correspond to the observation that occurred in the middle of each of the preheating phases, the highest temperature attained upon melting, a data point in the solidification regime, and the middle observation in the cooldown region. It is also noteworthy to mention that the double peaks shown in these spectral signal strength/emissivity plot in Fig. 3C), occurring in the range from 1347 to 1415 nm (highlighted as the semitransparent light blue region), are an effect of water vapor since the calibration was performed in air, as discussed by Fernandez *et. al.,* [12]. These values are not used in the calculation of temperature and do not represent the real target signal strength or emissivity values in this range. However, the authors chose to leave the data in this region to connect the data across the illustrated spectrum and to show at least one of the possible "environmental effects" on the measurements. The reader can ignore this region without loss of the impact of the work described here.

For comparison, Fig. 4 shows the temperature and signal strength/emissivity (at wavelength $\lambda = 1500$ nm) plots versus time during the powder preheating experiment, showing the data for the ten steps that consecutively increased the energy delivery using electron beam scanning. For Fig. 4, red horizontal lines indicate the melting range for the alloy, and blue horizontal lines show the maximum ($\varepsilon = 0.71$) and the lowest ($\varepsilon = 0.60$) signal strength or emissivity values reached for the first preheating cycle. These values serve as baselines to evaluate signal strength/emissivity changes in subsequent preheating cycles. Also, numbers are used in the figure to identify the preheating cycles. The first nine preheating cycles in this figure show increasing maximum temperature for each setting used, starting at a maximum temperature of 1150 °C in the first preheating cycle, to within the melting point for Inconel 625 (~1290 °C) for the ninth preheating cycle. Then the settings

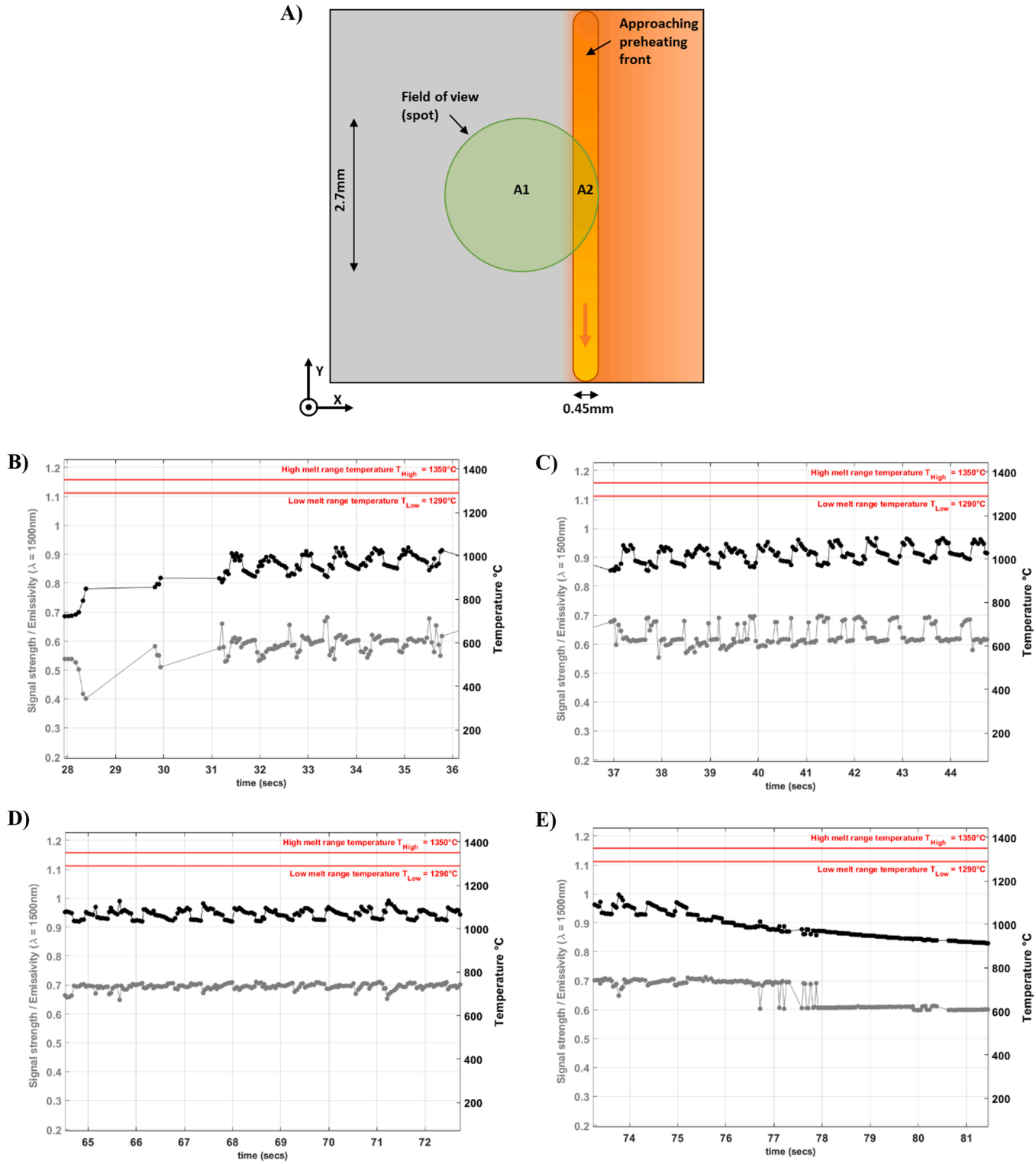

Fig. 6. A) Schematic showing the regions of different intensity as seen in the field of view of the FMPI during the approach of a preheating front. Zoomed-in regions of the plots for the first preheating cycle are shown to highlight initial drop in signal strength in B), the correspondence in temperature increases and signal strength decreases with changes in frequency in C) and D), and a transition in the signal strength/emissivity associated with metallic non-gray to gray transition of the target in E).

used for the last preheating step (tenth peak) elevate the temperature through the melting range and slightly above it. After melting, data were captured for the next 10 min during which temperature followed a descending trend towards 710 °C. At this point, the recording of data was stopped. The plot in gray reveals similar signal strength/emissivity behavior up to the sixth preheating step with maximum values at ~0.70 during preheating, followed by a drop in to ~0.60 during the local cooldown that follows each of these six preheating cycles. A decline in the signal strength/emissivity is seen in the subsequent four preheating cycles. For the seventh and eighth preheating cycles, peak signal

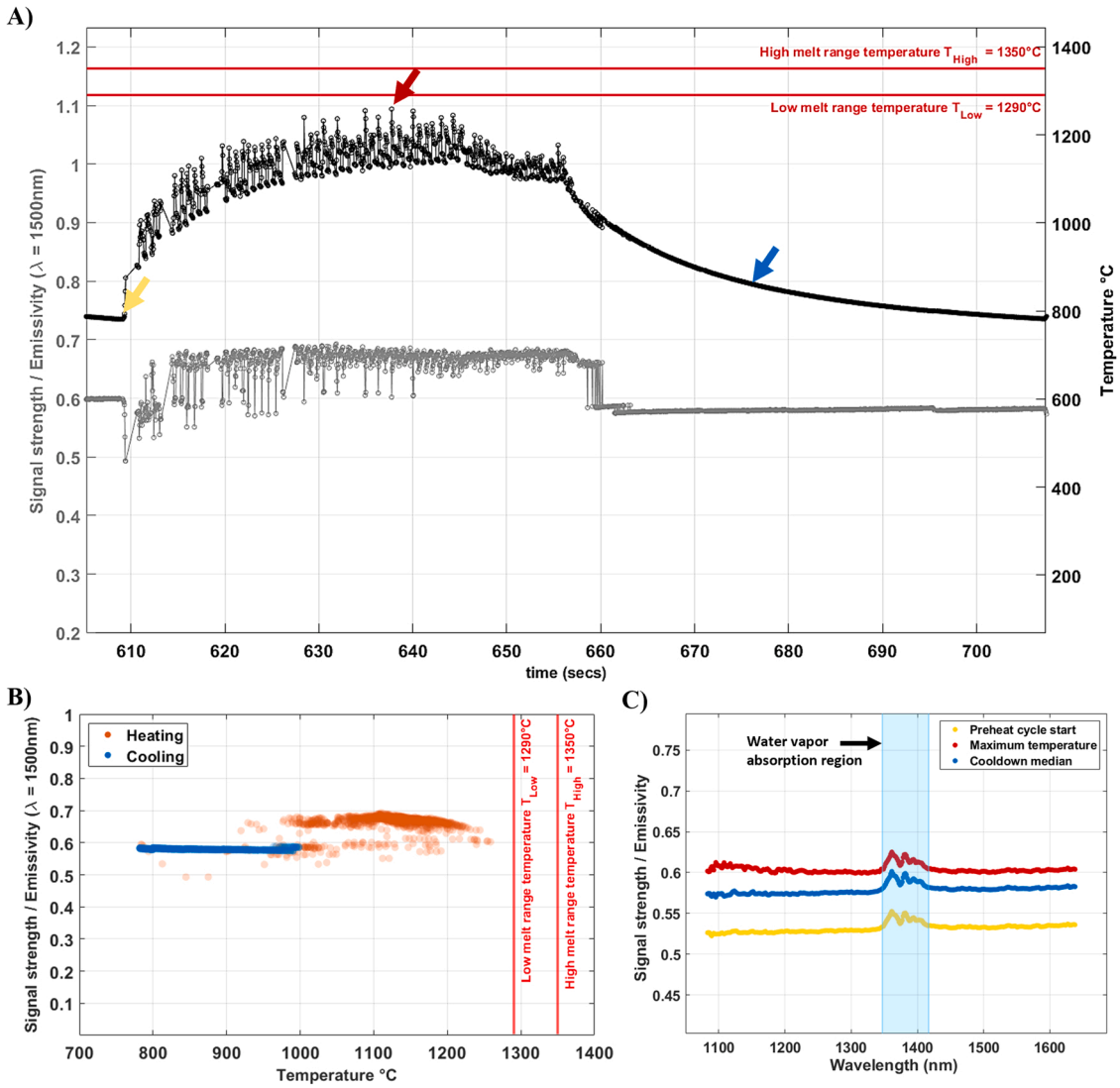

Fig. 7. Detail of temperature and emissivity plots for seventh (7th) preheating cycle. B) shows signal strength/emissivity versus temperature plot for heating and cooling, and C) shows spectral signal strength/emissivity at locations indicated by arrows in A).

strength/emissivity values are similar during preheating at ~0.67 and continue to lower to ~0.58 and ~0.55, respectively. In the ninth preheating cycle, as temperatures measured reached the melting range for the first time (i.e. T_{Low} = 1290 °C), signal strength/emissivity was ~0.58, declining afterwards to ~0.50. Finally, for the tenth preheating step, as the temperatures climbed above the melting range, the signal strength/emissivity values drop monotonically from ~0.55 to ~0.40, and then to ~0.35 during the last cooldown and for the remaining 10 min of the experiment. The emissivity values for this last cooldown are comparable to those in the cooldown in the regular melt (Fig. 2), with only slight differences (i.e. ~0.31 for the regular melt cooldown, and ~0.34 for the final cooldown in the preheat experiment) that are attributed to the differing surface morphologies on which observations are being made; while the hatch scanning employed during regular melting leads to characteristic surface texture that can indeed have an impact in the measured emissivity of a surface [24], the melting achieved through the preheating of the powder bed was visibly more amorphous as seen in SEM observations (Fig. 12–14) to be discussed in detail later.

Fig. 5 part A) shows detail of the temperature and signal strength/emissivity plots for various preheating cycles, part B) shows the signal strength/emissivity versus temperature plot for heating and cooling conditions, and part C) shows plots for spectral signal strength/emissivity at selected observation data points (indicated by color coded arrows) corresponding to the temperature during the start of the preheat cycle, the maximum measured temperature, and the median observation occurring in the cooldown. Similar plots are shown in Figs. 7–10 for preheating cycles 7th through 10th. For part B) in the previously mentioned figures, the transparency (alpha) value for markers was set at 0.25 to show datapoint overlap that help visualize the areas with more density of data and reveal the signal strength/emissivity trends. Also, the region of water vapor absorption comprising 1347–1415 nm is indicated in light semitransparent blue.

Fig. 5A) shows that the first preheating cycle starts slightly above ~750 °C and increases to the maximum temperature of ~1145 °C in about 30 s. During this time, signal strength/emissivity values make an excursion from a low of ~0.40 to a region with localized oscillations from ~0.60 to ~0.70. A characteristic slight drop in temperature is observed at t ~ 65 s corresponding with the start of the Stage II preheating step which results in reduced oscillations in both temperature (~1100 °C) and signal strength/emissivity values that cluster at ~0.70. Finally, on cooldown, the signal strength/emissivity falls and stays relatively constant at 0.60 towards the start of the next preheating cycle. As is evident in Fig. 4, though maximum temperatures are increasing during the five subsequent preheating cycles, the signal strength/emissivity trend is nearly identical. The similarity in the signal strength/

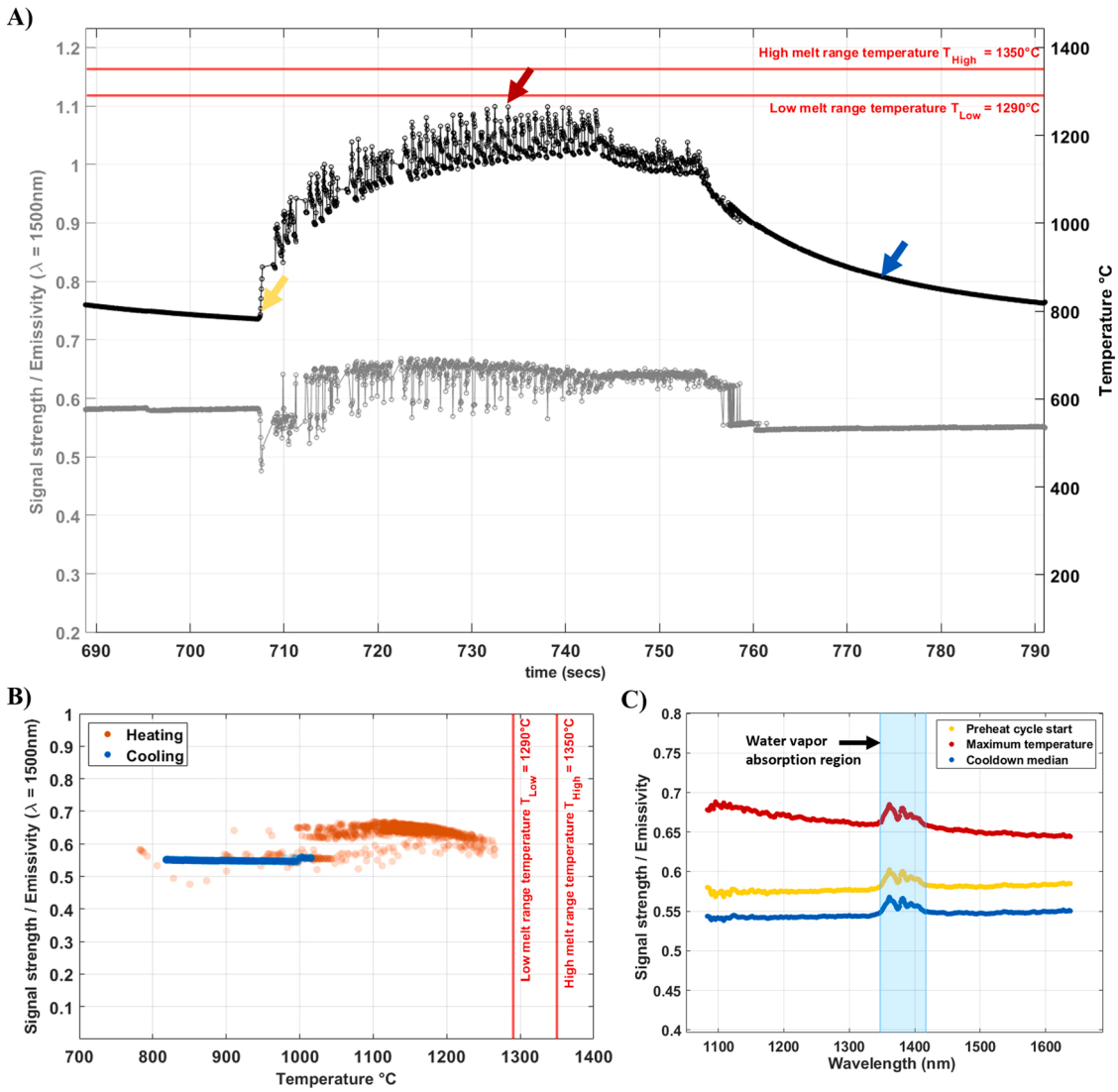

Fig. 8. A) Detail of temperature (black) and signal strength/emissivity (gray) plots for eighth (8th) preheating cycle. B) shows signal strength/emissivity versus temperature plot for heating and cooling, and C) shows spectral signal strength/emissivity at selected locations indicated by arrows in A).

emissivity trend is also shown in Fig. 5 B) for the first preheating cycle, which is representative of the first through sixth preheating cycles; in this plot, the signal strength/emissivity transitions through a region from ~0.60–0.70 during heating (temperature increase from ~950–1150 °C), then getting to a very stable value at ~0.60 during cooldown from ~975–750 °C.

Temporary decreases in signal strength/emissivity are effectively captured by the FMPI at the beginning of each preheating cycle, as exemplified in the drop to ~0.40 at t ~ 28 s shown in Fig. 5A), but also shown at the beginning of the other preheating cycles shown in parts A) for Figs. 7–10. The occurrence of this effect is associated with the uneven thermal conditions of the target during the approach of preheating fronts into the field of view (spot) of the FMPI. As shown schematically in Fig. 6A), as the first electron beam preheating front scans into the field of view, depicted as scanning from right to left, it locally heats up the partial area A2 while the rest of the area A1 remains at a lower temperature. Under this condition, and employing the analysis for two-color pyrometers by Ruffino [13], the temperature computed corresponds with the area of highest intensity (A2), while the corresponding signal strength calculated from the computed temperature and measured intensity is lower as it is more strongly influenced by A1 at a lower intensity. Once the field of view is more thermally homogeneous, the signal strength or emissivity increases to values that oscillate between ~0.50 and ~0.60 at the frequency of the electron beam scanning. As the temperature equilibrates in the field of view, the signal strength accurately represents the true emissivity of the target (according to the three conditions described previously).

The drop in signal strength/emissivity for the first preheating cycle is shown in the zoomed in region in Fig. 6B) at t ~ 28 s with the corresponding plot for temperature showing its increase as the electron beam scans into the field of view. It is also remarkable that the FMPI captures the local correspondence of the preheat scan fronts, raising the temperature and decreasing the signal strength as exemplified in Fig. 6C). In this plot, the frequency of the preheating wavefronts was measured at 1.72 Hz and it increased to 1.85 Hz during the second preheating stage which happened at higher scanning speed (Table 2), as shown in Fig. 6D). The frequency values measured correspond to the raster scanning of the electron beam with the line order parameter of 20 employed. Finally, the sensitivity of the FMPI was also demonstrated in its ability to capture a metallic non-gray transition during the cooldown phase seen in Fig. 6E). Comparing the data shown in the sequence of plots for Fig. 6, the oscillating behavior of signal strength/emissivity more characteristically seen in parts B) and C) and characteristically corresponding with non-gray behavior, subsides at time ~77 s to a

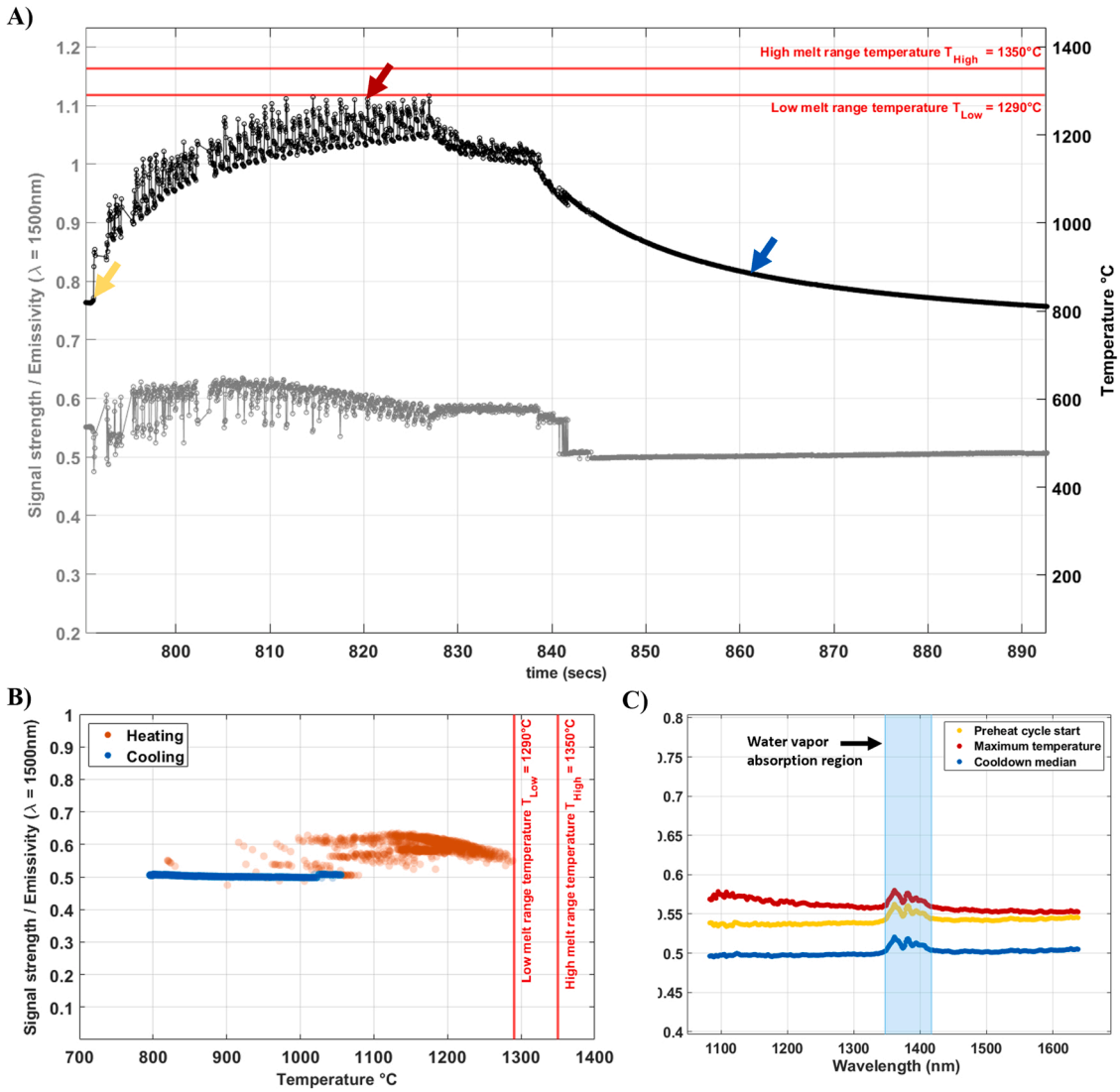

Fig. 9. Detail of temperature (black) and signal strength/emissivity (gray) plots for ninth (9th) preheating cycle. B) shows signal strength/emissivity versus temperature plot for heating and cooling, and C) shows spectral signal strength/emissivity at selected locations indicated by arrows in A).

stable value of ~0.60, indicating the transition into gray behavior.

Part A) in Figs. 7 and 8 show detailed plots for temperature and signal strength/emissivity for the seventh and eight preheating cycles, showing similar behaviors for temperature and signal strength/emissivity as in Fig. 5A). In Fig. 7A), the signal strength/emissivity values during heating are slightly under ~0.70 and these fall to just below ~0.60, during cooldown. Following into Fig. 8A), signal strength/emissivity continues a decline to values ~0.65 and 0.55 during heating and cooldown, respectively. Part B) in Fig. 8 provides the means to visualize that these signal strength/emissivity values cluster in the region comprising temperatures from 1000 °C-1250 °C during heating, and then from ~1000-800 °C during cooldown. The decline in the signal strength/emissivity values is hypothesized to be dominated by the change of morphology in the powder bed revealing the onset of sintering as induced by increased temperature, although chemistry changes might also be at interplay but were not directly measured.

Fig. 9A) for the ninth preheating cycle shows temperatures that reach into the reported melting range for alloy 625 for the first time (i.e., T_{Low} = 1290 °C). At t = ~800 s the signal strength/emissivity peaks at ~0.64 and then declines to ~0.59 for ~10 s to finally decrease to a stable value of ~0.5 during the cooldown for this preheating cycle. This excursion made by signal strength/emissivity as temperature increases is also evident in Fig. 9B) that shows a greater density of signal strength/emissivity data in the region ~0.65 at 1000 °C and that gradually decreases to ~0.60 at a temperature of ~1250 °C. Finally, Fig. 10A) shows temperature and signal strength/emissivity plots during the last preheating cycle. This plot reveals that as temperature increases close to the melting range, signal strength/emissivity peaks at ~0.56 then starts a gradual decrease by t = 920 s, finally stabilizing at ~0.40 by t = 975 s at which point the preheating by the electron beam stops. It is also noteworthy to mention the reduced oscillating behavior for the signal strength/emissivity plot, when temperatures are consistently in the melting range (from t = 940 s to t = 975 s), which suggests the observations are recorded for a material with morphology increasingly more homogeneous, indicating the onset of melting. The evidence of melting is seen in the last trend of signal strength/emissivity (Fig. 10) with values that remain at ~0.35 during cooldown and until the end of the experiment.

Fig. 9B) shows that during heating in the wide temperature range from ~1050 °C to ~1300 °C signal strength/emissivity varies in a region from ~0.55 to ~0.63, with a region with high density values concentrating at ~0.60. During cooling from temperatures ~1050 °C and down to ~790 °C, signal strength/emissivity remains stable at ~0.50.

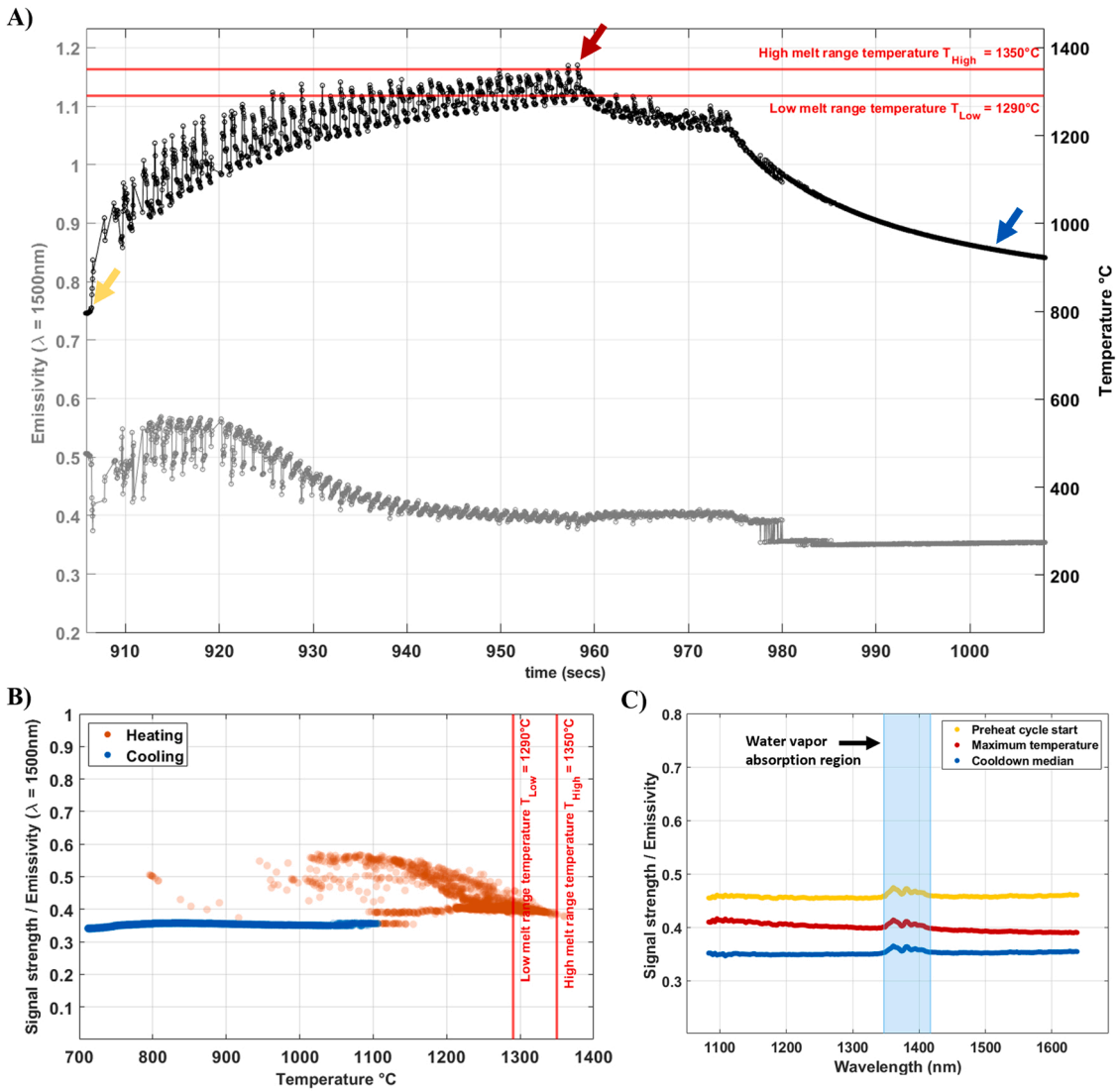

Fig. 10. Detail of temperature (black) and signal strength/emissivity (gray) plots for tenth (10th) preheating cycle. B) shows signal strength/emissivity versus temperature plot for heating and cooling, and C) shows spectral signal strength/emissivity at selected locations.

The signal strength/emissivity transitions from the 5th through 10th preheating cycles are shown in Fig. 11. In this plot, blue dashed arrows have been added to indicate the progression of maximum (during preheat) and minimum (during cooldown) signal strength/emissivity values recorded. Only small decreases in the signal strength/emissivity occurred from the fifth to the sixth preheating cycles, but these changes are more drastic starting in the seventh preheating cycle, and specifically evident during cooldown. For example, at the onset of cooldown in the seventh preheat cycle, the decrease is from 0.60 baseline to 0.57. This decreasing trend continues to a value of 0.54 at the eighth preheating cycle, 0.50 at the ninth preheating cycle, and ultimately 0.35 for the cooldown following the tenth preheating cycle before the end of the experiment. The decrease in maximum signal strength/emissivity values is also more pronounced from the eighth preheating cycle to the tenth, with corresponding values of 0.67, 0.64, and 0.57. The rather abrupt change in signal strength/emissivity values, starting in the seventh, and ending into the tenth preheating cycles, indicates that in addition to the increase in temperature, secondary factors are influencing the signal strength/emissivity values calculated. Given the controlled conditions inside the vacuum of PBF-EB and accounting for the reduced influence of the radiation environment, as detailed in [12], it is hypothesized that this behavior can be mostly attributed to the occurrence of changes in morphology and phase in the powder bed as increased sintering is developing, leading up to the eventual melting and solidification of the material, although the potential effects of chemistry changes cannot be removed as this was not experimentally measured or controlled. The results obtained indicate the ability of the presented MW technique to reveal the phase and morphology changes during PBF processing conditions. The morphology changes for these phase transitions are illustrated in the SEM microscopy performed as discussed in Section 3.2.

In our observations, the signal strength/emissivity values are dynamic in nature, and they generally decrease as temperature increases. Nonetheless, during the preheating stages, the oscillating behavior showing an increase-decrease trend, correspond to the localized heating wavefronts that developed by the electron beam preheating raster scanning strategy; a process effect that is remarkably captured by the FMPI. The signal strength/emissivity behavior shown and described previously is consistent with data reported in the Thermophysical Properties of Matter (TPRC Vol 7) compendium [25] for various metal samples in a variety of conditions. Also, in our prior work using the FMPI with pure copper, a similar decreasing signal strength/emissivity was seen upon reaching melting of the material [12], and during vacuum induction melting for Inconel 718 [26]. Further, although the literature about emissivity of nickel-based alloys in PBF AM is sparse, several

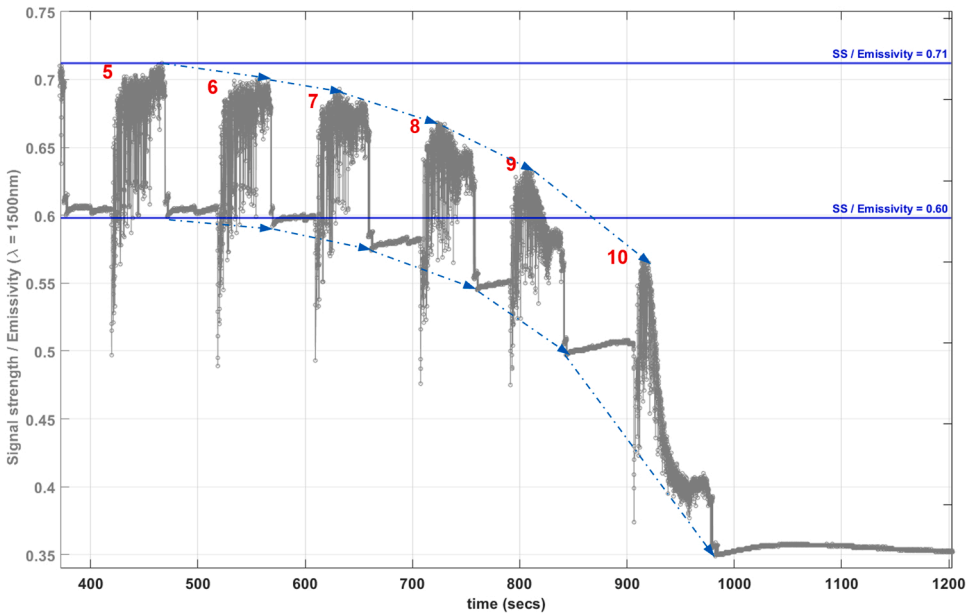

Fig. 11. Zoomed in plot for signal strength/emissivity at $\lambda = 1500$ nm from the end of the fourth through the tenth preheating cycles. Blue horizontal lines show the maximum signal strength/emissivity during preheating and minimum during cooldown. Dashed arrows serve to indicate the emissivity decrease in each subsequent preheating cycle. Red numbers indicate each preheating cycle.

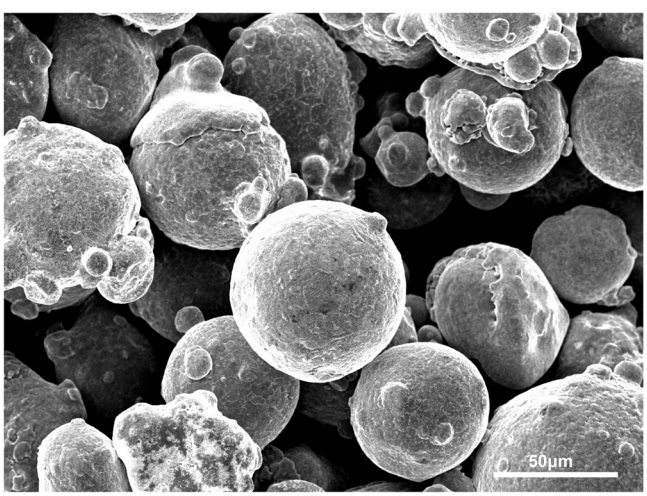

Fig. 12. 500X magnification micrograph for compacted powder collected from a region of the powder bed following a regular fabrication in PBF-EB.

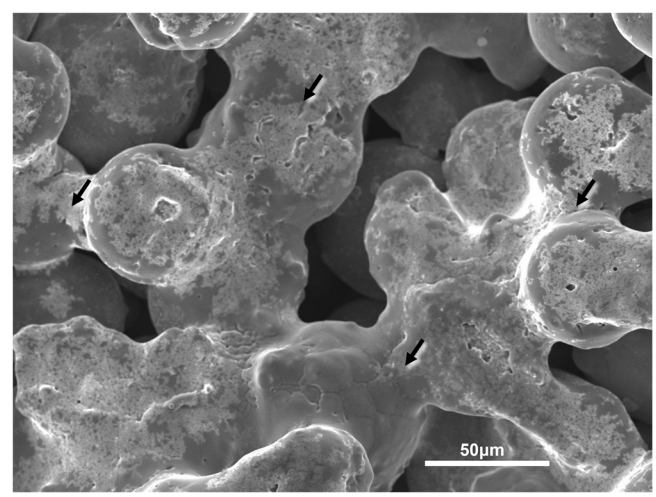

Fig. 13. 500X magnification micrograph for powder collected from a region of the powder bed that was subjected to seven consecutive preheating cycles. Sintering is illustrated by the formation of multiple necks and coalesced particles; several of these features are indicated by arrows. Also, notice absence of satellite and smaller particles.

related works have shown the emissivity behavior for these alloys, mostly in the study of structural materials suitable for nuclear reactors. For example, values for emissivity obtained from heating of solid specimens made of several nickel base alloys, using concentrated solar radiation under vacuum, show a decrease in total hemispherical emissivity from ~0.40 at 1100 K down to ~0.25 at the maximum temperature of testing of 1300 K. This behavior was shown for several alloys including Inconel 600, Inconel 690, Hastelloy X, Haynes 230, and Haynes HR120 [27]. Similarly, the same method as in [27] was employed to measure the total hemispherical emissivity for 316 L, showing that emissivity gradually decreases from ~0.40 at 1100 K to ~0.28 near 1400 K [28]. By contrast, heating of solid Inconel 718 samples in the temperature range from 750 to 1400 K showed a gradual increase in emissivity from ~0.20 to ~0.28, albeit for solid samples that were heated below the melting range of the alloy, stated at 1483–1617 K [29]. It is instructive to recall that the measurements performed in this work were done for heated metal powder, which do not readily compare with results in literature usually consisting of prepared solid metal (disc) samples. These differences in morphology and temperature ranges, clearly separate the results obtained here versus those reported elsewhere.

3.2. Morphological changes to powder

Samples of preheated powders were collected and analyzed under SEM to document the evidence of sintering and melting. For comparison, a sample was also collected from the powder bed after a regular build in PBF-EB. Fig. 12 shows the compacted powder that had undergone the regular build at x500 magnification. Comparison of Fig. 12 with the inset in Fig. 1 reveals no drastic change in the powder morphology following the preheating sequences during the regular fabrication; qualitatively, the powder retains its original morphology, with the

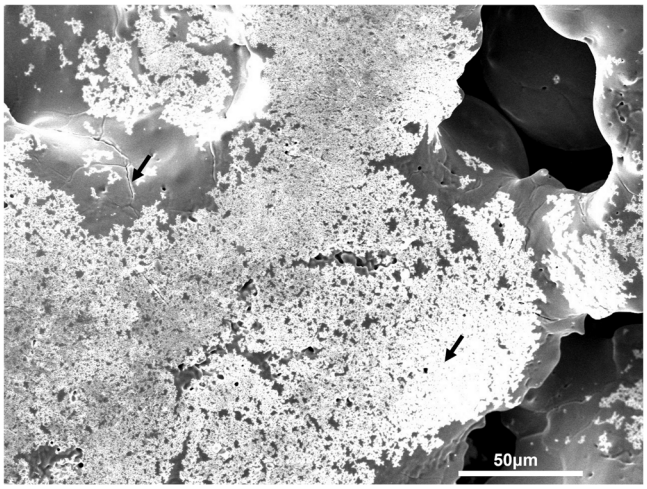

Fig. 14. 500X magnification micrograph showing a region of material that was melted following sustained preheating up to the tenth preheating cycle. Illustrations of melting and subsequent solidification includes micro-dendritic formations and cracking, annotated with arrows.

occurrence of mostly spheroidal particles with satellites. This is expected since a given layer of powder only experiences a single direct preheating by the electron beam thus reducing the time and energy available to induce sintering. The electron beam process parameters used in a regular fabrication in PBF-EB, achieve compaction of the powder for process stability, but this normal preheating step does not last long enough to induce sintering.

By contrast, the SEM image in Fig. 13 shows the effect of the sustained preheating cycles, as performed in the work reported here, with more evidence of sintering, including the formation of particle-particle necks, and clusters of various coalesced particles, as indicated by arrows in the figure. Several works in literature have studied the sintering effect induced by electron beam preheating in PBF-EB, mostly for Ti6Al4V, showing comparable sintering and partial melting as reported in our work. For example, the sintering mechanism during preheating in PBF-EB was recently detailed in [30], showing the formation of inter-particle necking. Also, consistent with our observations, the sintering of Ti6Al4V powder was carried out in the work of Smith *et. al.* [31], concluding that higher interconnectivity and partial melting were correlated with a higher number of electron beam passes or scans that subsequently elevated the temperature. Furthermore, He *et. al.* [32] described that the sintering mechanism during preheating of Ti6Al4V involved the partial or complete melting of the smaller particles to serve as a binder hence reducing their prevalence; a conclusion that is consistent with our observations of reduced occurrence of smaller particles and satellites, as shown in Fig. 13.

The SEM image in Fig. 14 reveals that following sintering, the subsequent preheating ocurring during the ninth and tenth preheating cycles, caused localized melting; this is illustrated in the figure as regions of interconnected solidified material not showing the features of the starting spheroidal particle, and satellite morphology. A discontinuous molten surface is shown in Fig. 13 indicating the development of micro-dendritic solidification and surface cracking, annotated by arrows.

4. Conclusions

The experiment presented in this work employed multi-wavelength pyrometry using a commercial device operating in the active range from 1080 to 1637 nm, to capture changing signal strength/emissivity values as the signature of phase transitions, including sintering and melting, during sustained preheating of an Inconel 625 powder bed. The presented approach highlights a MW pyrometry technique that can be used as an in situ diagnostic tool, capable of revealing the development of processing stages occurring in PBF AM, and likely for other thermally driven materials processing methods. Improvements to the MW pyrometer employed are required to attain higher spatial and temporal resolution, specifically to capture more detail of the transient non-equilibrium solidification conditions at smaller length scales (i.e. melt-pool) of interest in PBF-EB. However, the results described here have shown the MW pyrometer has remarkable sensitivity to detect, under controlled environmental conditions, the dynamic thermal signal strength/emissive transitions of materials clearly associated with morphology transformations, but also in response to temperature, phase, and although not directly controlled, for chemistry variations. For example, for the measurements reported as the target underwent melting, the device resolved measurements with an acquisition time in the range from 0.006 to 0.012 s, enough to observe the signal strength or emissivity transitions during this phase transition. The sensitivity of the FMPI in its current configuration was shown capable of capturing the preheating wavefronts created by the raster scanning with the electron beam, and the respective changes in the signal strength (emissivity), as exemplified in the initial decrease in signal strength observed at the beginning of each of the preheating cycles.

Sharp transitions in the signal strength or emissivity at the wavelength $\lambda = 1500$ nm were observed as the temperature continued to elevate. These drastic changes at the onset of sintering and melting, especially during the seventh preheating cycle onwards, concurrent with temperature increases, were correlated with the loss of the starting powder morphology (sphericity and satellite) into a morphology exhibiting sintering and melting characteristics, as seen in SEM images. Besides this, the technique presented could also be used, under controlled experimental conditions, to detect the emissivity changes associated with chemistry variations in powder feedstocks employed in PBF AM due to reuse cycles.

Future work is concentrating on improvements to the MW pyrometry technique, including increasing the time resolution of the device, and the development of optics with increased spatial resolution, ideally to the dimensions of the melt-pool. These advances would help to further enhance our understanding of the interactions between the energy source and the powder, and of the emissive behavior of materials during phase transitions induced in PBF AM, to improve thermal monitoring techniques for these processes. Also, although not directly the subject of the current manuscript, it is worth restating the spectral nature of signal strength/emissivity, as shown in the part C) in Figs. 5 and 7 through 10 that has implications for thermal monitoring in PBF AM, as also detailed in prior work [12]. Current research efforts on this subject are underway and will be presented in subsequent works in more detail for several alloys of interest for PBF AM.

CRediT authorship contribution statement

Cesar Adrian Terrazas Najera: Writing – review & editing, Writing – original draft, Visualization, Methodology, Investigation, Formal analysis, Data curation, Conceptualization. **Alejandro Romero:** Methodology, Investigation. **Ralph Felice**: Writing – review & editing, Validation, Investigation, Formal analysis. **Ryan Wicker:** Writing – review & editing, Validation, Supervision, Resources, Project administration, Investigation, Funding acquisition, Formal analysis, Conceptualization.

Declaration of Competing Interest

The authors declare that they have no known competing financial interests or personal relationships that could have appeared to influence the work reported in this paper.

Data Availability

Data will be made available on request.

Acknowledgements

The research described here was performed at The University of Texas at El Paso (UTEP) within the W.M. Keck Center for 3D Innovation (Keck Center). The authors are grateful to Kurtis Watanabe and Alex De La Cruz, as well as Dr. Francisco Medina for providing support for the experiments presented in this work. This material is based on research sponsored by, in part, the Air Force Research Laboratory (AFRL) under agreement number FA8650–20-2–5700. Additional support was provided by strategic investments via discretionary UTEP Keck Center funds and the Mr. and Mrs. MacIntosh Murchison Chair I in Engineering Endowment at UTEP. The U.S. Government is authorized to reproduce and distribute reprints for Governmental purposes notwithstanding any copyright notation thereon. The views and conclusions contained herein are those of the authors and should not be interpreted as necessarily representing the official policies or endorsements, either expressed or implied, of AFRL or the U.S. Government.

References

[1] W.J. Sames, F.A. List, S. Pannala, R.R. Dehoff, S.S. Babu, The metallurgy and processing science of metal additive manufacturing, Int. Mater. Rev. ISSN (2016).
[2] K. Amato, J. Hernandez, L.E. Murr, E. Martinez, S.M. Gaytan, P.W. Shindo, S. Collins, Comparison of microstructures and properties for a Ni-base superalloy (Alloy 625) fabricated by electron beam melting, J. Mater. Sci. Res. 1 (2012) 3, https://doi.org/10.5539/jmsr.v1n2p3.
[3] J. Varela, J. Merino, C. Pickett, A. Abu-Issa, E. Arrieta, L.E. Murr, R.B. Wicker, M. Ahlfors, D. Godfrey, F. Medina, Performance characterization of laser powder bed fusion fabricated inconel 718 treated with experimental hot isostatic processing cycles, J. Manuf. Mater. Process. 4 (2020) 73, https://doi.org/10.3390/JMMP4030073.
[4] B.A. Fisher, J. Mireles, S. Ridwan, R.B. Wicker, J. Beuth, Consequences of part temperature variability in electron beam melting of Ti-6Al-4V, JOM 69 (2017) 2745–2750, https://doi.org/10.1007/s11837-017-2597-y.
[5] P.M. Cordero, J. Mireles, S. Ridwan, R.B. Wicker, Evaluation of monitoring methods for electron beam melting powder bed fusion additive manufacturing technology, Prog. Addit. Manuf. 2 (2017) 1–10, https://doi.org/10.1007/s40964-016-0015-6.
[6] J. Raplee, A. Plotkowski, M.M. Kirka, R. Dinwiddie, A. Okello, R.R. Dehoff, S. S. Babu, Thermographic microstructure monitoring in electron beam additive manufacturing, Sci. Rep. 7 (2017) 1–16, https://doi.org/10.1038/srep43554.
[7] J. Mireles, C. Terrazas, S.M. Gaytan, D.A. Roberson, R.B. Wicker, Closed-loop automatic feedback control in electron beam melting, Int. J. Adv. Manuf. Technol. (2014), https://doi.org/10.1007/s00170-014-6708-4.
[8] E. Rodriguez, J. Mireles, C.A. Terrazas, D. Espalin, M.A. Perez, R.B. Wicker, Approximation of absolute surface temperature measurements of powder bed fusion additive manufacturing technology using in situ infrared thermography, Addit. Manuf. 5 (2015), https://doi.org/10.1016/j.addma.2014.12.001.
[9] N. Boone, C. Zhu, C. Smith, I. Todd, J.R. Willmott, Thermal near infrared monitoring system for electron beam melting with emissivity tracking, Addit. Manuf. 22 (2018) 601–605, https://doi.org/10.1016/j.addma.2018.06.004.
[10] P.A. Hooper, Melt pool temperature and cooling rates in laser powder bed fusion, Addit. Manuf. 22 (2018) 548–559, https://doi.org/10.1016/j.addma.2018.05.032.
[11] M. Vollmer, K.P. Möllmann, Infrared thermal imaging: fundamentals, research and applications, Wiley Blackwell, Weinheim, Germany, 2017, https://doi.org/10.1002/9783527693306.
[12] A. Fernandez, R. Felice, C.A. Terrazas, R. Wicker, Implications for accurate surface temperature monitoring in powder bed fusion: using multi-wavelength pyrometry to characterize spectral emissivity during processing, Addit. Manuf. (2021), 102138, https://doi.org/10.1016/j.addma.2021.102138.
[13] G. Ruffino, Two-colour pyrometry on nonisothermal fields: a measurement problem in siderurgy, High. Temp. High. Press 6 (1974) 223–227.
[14] R. German. Sintering: From Empirical Observations to Scientific Principles, Elsevier, 2014, pp. 1–536, https://doi.org/10.1016/C2012-0-00717-X.
[15] S.J.L. Kang, Sintering: Densification, grain growth and microstructure. *Sintering: Densification*, Grain Growth and Microstructure (2005) 1–265. https://doi.org/10.1016/B978-0-7506-6385-4.X5000-6.
[16] M. Galati, L. Iuliano, A literature review of powder-based electron beam melting focusing on numerical simulations, Addit. Manuf. 19 (2018) 1–20, https://doi.org/10.1016/J.ADDMA.2017.11.001.
[17] L.E. Murr, E. Martinez, K.N. Amato, S.M. Gaytan, J. Hernandez, D.A. Ramirez, P. W. Shindo, F. Medina, R.B. Wicker, Fabrication of metal and alloy components by additive manufacturing: Examples of 3D materials science, J. Mater. Res. Technol. 1 (2012) 42–54, https://doi.org/10.1016/S2238-7854(12)70009-1.
[18] E. Martinez, L.E. Murr, K.N. Amato, J. Hernandez, P.W. Shindo, S.M. Gaytan, D. A. Ramirez, F. Medina, R.B. Wicker, 3D microstructural architectures for metal and alloy components fabricated by 3D printing/additive manufacturing technologies, 1st Int. Conf. 3D Mater. Sci. 2012 (2012) 73–78, https://doi.org/10.1007/978-3-319-48762-5_11.
[19] F.A. List, R.R. Dehoff, L.E. Lowe, W.J. Sames, Properties of Inconel 625 mesh structures grown by electron beam additive manufacturing, Mater. Sci. Eng.: A 615 (2014) 191–197, https://doi.org/10.1016/J.MSEA.2014.07.051.
[20] J.A. Gonzalez, J. Mireles, S.W. Stafford, M.A. Perez, C.A. Terrazas, R.B. Wicker, Characterization of Inconel 625 fabricated using powder-bed-based additive manufacturing technologies, J. Mater. Process Technol. 264 (2019) 200–210, https://doi.org/10.1016/j.jmatprotec.2018.08.031.
[21] R.A. Felice, Temperature Determining Device and Process, US 5,772,323, 1998.
[22] R.A. Felice, The Spectropyrometer – a Practical Multi-wavelength Pyrometer, in: 8th Symposium on Temperature: Its Measurement and Control in Science and Industry, AIP, 2002.
[23] R.A. Felice, Temperature Determining Device and Process, US 6,379,038 B1, 2002.
[24] S. Taylor, J.B. Wright, E.C. Forrest, B. Jared, J. Koepke, J. Beaman, Investigating relationship between surface topography and emissivity of metallic additively manufactured parts, Int. Commun. Heat. Mass Transf. 115 (2020), 104614, https://doi.org/10.1016/j.icheatmasstransfer.2020.104614.
[25] Y.S. Tolukian, D.P. DeWitt, Thermal Radiative Properties - Metallic Elements and alloys, Thermophysical Properties of Matter (1970).
[26] D.M. Olinger, R.A. Felice, J. v Gray, Successful Pyrometry in Investment Casting, Investment Casting Institute 55th Technical Conference and Expo. (2007).
[27] M. Balat-Pichelin, J.L. Sans, E. Bêche, L. Charpentier, A. Ferrière, S. Chomette, Emissivity at high temperature of Ni-based superalloys for the design of solar receivers for future tower power plants, Sol. Energy Mater. Sol. Cells 227 (2021), 111066, https://doi.org/10.1016/J.SOLMAT.2021.111066.
[28] M. Balat-Pichelin, J.L. Sans, E. Bêche, Spectral directional and total hemispherical emissivity of virgin and oxidized 316L stainless steel from 1000 to 1650 K, Infrared Phys. Technol. 123 (2022), 104156, https://doi.org/10.1016/J.INFRARED.2022.104156.
[29] B.P. Keller, S.E. Nelson, K.L. Walton, T.K. Ghosh, R. v Tompson, S.K. Loyalka, Total hemispherical emissivity of Inconel 718, Nucl. Eng. Des. 287 (2015) 11–18, https://doi.org/10.1016/J.NUCENGDES.2015.02.018.
[30] W. Yan, W. Ma, Y. Shen, Powder sintering mechanisms during the pre-heating procedure of electron beam additive manufacturing, Mater. Today Commun. 25 (2020), 101579, https://doi.org/10.1016/j.mtcomm.2020.101579.
[31] C.J. Smith, S. Tammas-Williams, E. Hernandez-Nava, I. Todd, Tailoring the thermal conductivity of the powder bed in Electron Beam Melting (EBM) Additive Manufacturing, Sci. Rep. 2017 7:1. 7 (2017) 1–8, https://doi.org/10.1038/s41598-017-11243-8.
[32] W. He, W. Jia, H. Liu, H. Tang, X. Kang, Y. Huang, Research on Preheating of Titanium Alloy Powder in Electron Beam Melting Technology, Rare Met. Mater. Eng. 40 (2011) 2072–2075, https://doi.org/10.1016/S1875-5372(12)60014-9.